LANGMUIR

pubs.acs.org/Langmuir Article

Rheological Characteristics of Ionic Liquids under Nanoconfinement

Mengwei Han, Simon A. Rogers, and Rosa M. Espinosa-Marzal*



Cite This: Langmuir 2022, 38, 2961–2971



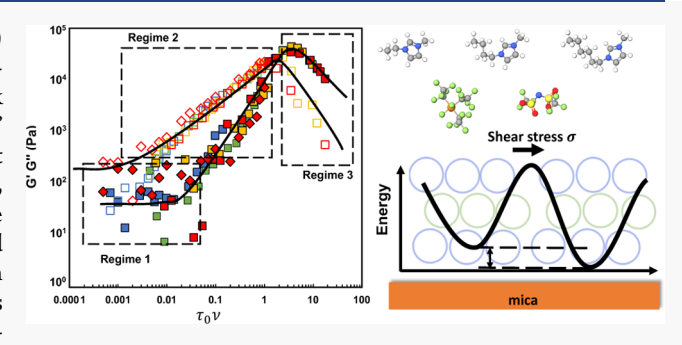
ACCESS I

Metrics & More

Article Recommendations

S Supporting Information

ABSTRACT: While the dynamic properties of ionic liquids (ILs) in nanoconfinement play a crucial role in the performance of IL-based electrochemical and mechanical devices, experimental work mostly falls short at reporting "solid-like" versus "liquid-like" behavior of confined ILs. The present work is the first to conduct frequency-sweep oscillatory-shear rheology on IL nanofilms, reconciling the solid-versus-liquid debate and revealing the importance of shear rate in the behavior. We disentangle and analyze the viscoelasticity of nanoconfined ILs and shed light on their relaxation mechanisms. Furthermore, a master curve describes the scaling of the dynamic behavior of four (non-hydrogen-



bonding) ILs under nanoconfinement and reveals the role of the compressibility of the flow units.

INTRODUCTION

The dynamics of ionic liquids (ILs) in nanoconfinement and at the solid—liquid interface has been under continued scrutiny for its relevance to applications in energy storage^{1–4} and lubrication.^{5,6} The use of ILs in electrochemical devices, such as supercapacitors, is hindered by their low conductivity, which is detrimental to the power density of the device. The disadvantage of sluggish dynamics may be further exacerbated by the presence of nanopores in the electrodes intended to maximize specific capacitance. While reduced mobility of ILs in nanopores is expected,^{7,8} some counter evidence points at an enhancement of IL diffusivity in nanoconfinement, which indicates the complexity of the underlying mechanisms.^{9,10} In the context of lubrication, the rheological properties of the lubricant trapped between the two sliding surfaces significantly affect friction and thereby the energy loss.

It has been widely reported that IL ions organize in layers near a charged surface. Lextensive efforts have been made to investigate structural and dynamic properties of ILs near a solid interface as well as the influence of nanoconfinement using spectroscopy, Leave Tay reflectivity, neutron scattering, NMR, and electrochemical techniques. Nanomechanical methods have provided unique perspectives about the transition of IL behavior upon nanoconfinement toward elastic or solid behavior, which is often referred to as solid-like behavior. For example, the mechanical impedance of 1-butyl-3-methylimidazolium tetrafluoroborate (abbreviated as [BMIM]-[BF4]) measured under the excitation of a tuning-fork-based atomic force microscope suggested that the interfacial film exhibits a change of properties toward a solid-like phase below a threshold thickness, pointing to capillary freezing or crystallization in confinement. The threshold is related to the metallic nature of the confining surfaces, with more metallic surfaces

facilitating freezing.²² The thickness and the mechanical impedance of the film are both substrate- and voltagedependent.²³ In a different work, the damping of an atomic force microscopy (AFM) tip excited magnetically in the lateral direction revealed interfacial ordering and solidification of the IL ions bound to a biased gold surface.²⁴ Due to the unrivaled advantages of precisely determining and controlling the thickness of nanoconfined ILs, the surface force apparatus (SFA)-based techniques have been re-designed to carry out nanorheological tests. Thus, using the so-called dynamic SFA, 1-butyl-3-methylimidazolium hexafluorophosphate (abbreviated as [BMIM][PF₆]) was found to be ordered in layers at the solid—liquid interface and reciprocal shear revealed an orderof-magnitude increase in shear stress with decreasing film thickness of the nanoconfined IL.²⁶ Resonance shear measurements revealed an increase of viscosity of [BMIM][PF₆] and [BMIM][BF₄] upon nanoconfinement, 27 while in situ X-ray diffraction discovered a possible transition in the scattering pattern under confinement that could explain structural and viscosity changes of the ILs.²⁸ By measuring the squeeze-out events of nanoconfined ILs, our group has also reported the remarkable increase of effective viscosity²⁹ and that this increase can be reduced by the presence of a trace amount of water.³⁰ Despite these and other studies specifically focused on ILs near mica surfaces,³¹ the mechanisms governing the mobility of the IL ions are still unclear and the relation between molecular

Received: December 27, 2021 Revised: February 10, 2022 Published: February 27, 2022





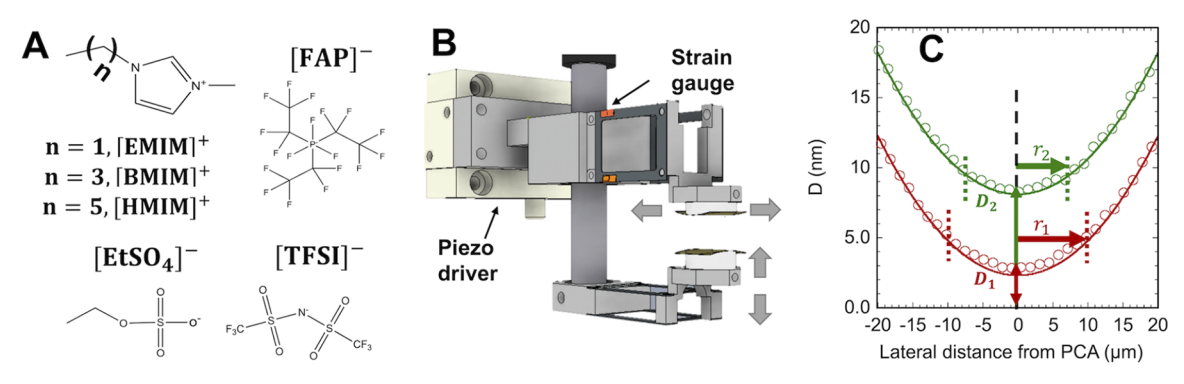


Figure 1. Schematics of the instrument, ionic liquids, and contact geometry. (A) Chemical structures of investigated IL cations and anions; (B) schematics of the nanorheometer used in this study; (C) surface profile obtained by scanning the spectrometer around the point of closest approach. The center of the profile is flattened due to the normal pressure. The radius of the deformed area is estimated and used to calculate the geometrical factor Ω .

structure and dynamic behavior at interfaces and under nanoconfinement remains elusive.

Frequency-dependent oscillatory shear rheology coupled with an SFA is a powerful tool for understanding relaxation mechanisms of fluids. Here, this method was used to shed light on the mechanisms governing the dynamics of ILs under nanoconfinement. We report oscillatory shear measurements with an extended SFA over a frequency range of 3 decades for five imidazolium IL thin films and reveal significant differences in the rheological behavior before and after an IL layer is squeezed out. We propose a master curve with three distinct regions at low, intermediate, and high Deborah numbers to describe the rheological behavior of nanoconfined ILs without strong hydrogen-bonding capabilities.

■ EXPERIMENTAL SECTION

The objective of the study was to measure and compare the rheological behavior of various ILs confined between mica surfaces using an extended SFA. The use of an SFA is key because it enables to control the thickness of the IL films with Å precision. Five imidazolium ILs were selected for this study, namely, 1-ethyl-3-methylimidazolium bis(trifluoromethyl sulfonyl)imide (abbreviated [EMIM][TFSI]), 1-butyl-3-methylimidazolium bis(trifluoromethyl sulfonyl)imide (abbreviated [BMIM][TFSI]), 1-hexyl-3-methylimidazolium bis(trifluoromethyl sulfonyl)imide (abbreviated [HMIM][TFSI]), 1-ethyl-3-methylimidazolium ethyl sulfate (abbreviated [EMIM][EtSO_4]), and 1-ethyl-3-methylimidazolium tris(pentafluoroethyl)-trifluoro-phosphate (abbreviated [EMIM][FAP]). The selected imidazolium ILs are some of the most investigated ILs at interfaces (Figure 1A). The experimental study required to avoid water contamination during the duration of the experiment.

MATERIALS

All chemicals were purchased from Millipore Sigma (MO, USA), and small aliquots of \sim 500 μ L were dried in vials under vacuum at 50 $^{\circ}$ C for 48 h before use.

Surface Force Apparatus. A number of improvements for thermal and mechanical stability and resolution have been implemented in our SFA, which are detailed elsewhere. 36,37 Mica (Optical grade # 1, S&J Trading, NY) was manually cleaved into roughly 1 cm by 1 cm sheets with a thickness of $2-6~\mu m$ and back-coated with 40 nm silver using an e-beam evaporator. Mica sheets of equal thicknesses were glued onto two curved glass discs with a radius of curvature R of 2 cm using an epoxy glue (Epon 1004 F). Mica pairs were positioned such that the principal crystallographic axes are perpendicular to each other. A volume of ~200 μL was injected into the space between the two surfaces. After equilibrating overnight, surface force measurements were conducted at a velocity of 0.5 nm/s. All experiments were

performed at 25 \pm 0.02 °C and under a protective N_2 atmosphere with 0% relative humidity, monitored with a humidity sensor (SHT75, Sensirion, Switzerland).

The SFA was modified to perform nanorheological measurements, and the schematics are shown in Figure 1B. The relative motion in the lateral direction is enabled using a P754 piezoelectric actuator (Physik Instrumente, Germany) modulated by a E-754 controller (Physik Instrumente, Germany). A pair of springs connects the holder of the glass lens to the piezo, the deflection of which is measured through four strain gauges (FLK-1-11-3LJCT, Texas Measurements, College Station, TX) configured into a full Wheatstone bridge. The voltage output of the full-bridge transducer is measured using a data acquisition system (Pacific Instrument, Concord, CA) with a time resolution of 0.04 ms. The conversion factor between the voltage and the deflection on the spring is obtained by connecting the disc holders with a rigid metal rod and measuring the voltage reading when the piezo driver is moved by a known distance, and it is $K_2 = 7.1 \times 10^{-5}$ m/mV. The stiffness of the normal spring (K_n) was determined by calibration against a known weight and measuring the cantilever deflection with a pocket microscope, yielding $K_n = 1000 \text{ N/m}$. The constant of the lateral spring $(K_r = 356 \text{ N/m})$ was determined by applying a known force on the spring assembly and reading the voltage and deflection.

In nanorheological measurements, the piezo moves following a cosine wave. The controller sends a trigger voltage to the data acquisition system no later than 0.1 ms after the piezo motion starts, which synchronizes piezo motion and the measurement of voltage output. Thus, the resolution in time is defined as 0.1 ms, which is smaller than the time scales probed in this work. The resonance frequency of the device is $\sim 30-40$ Hz, which limits the maximum experimental frequency; see the calibration data in Figure S1. Hence, in frequency-sweep tests, the amplitude of the piezo motion, A_0 , was set to 1000 nm, while the frequency, ν , was varied from 0.01 to 20 Hz. Amplitude sweeps were conducted at the selected frequencies (0.01, 0.1, 1, and 10 Hz) with A_0 ranging from 500 to 1800 nm. It is worth pointing out that the strain applied on the IL is much smaller than the piezo motion (A_0) since the spring deflects.

Rheological Analysis. The goal of the rheological measurements is to obtain insight into the properties of the nanoconfined ILs, which requires solving the equation of motion. While our setup was inspired by Luengo et al., $^{2.5}$ it exhibits certain differences, which are reflected in a different equation of motion. The equation of motion for the surface connected to the piezo results from the balance between the spring force, $K_x \times \delta$, and the friction force, $\eta \times \Omega \times V$, against the motion of the surface

$$K_x \times \delta - \eta \times \Omega \times V = 0 \tag{1}$$

where η is the viscosity of the confined liquid, Ω is a geometric factor based on Reynold's lubrication theory (for a sphere moving laterally along a flat surface or for parallel plates), and V the relative velocity between the two mica surfaces. The surface displacement x is given as

Table 1. Frequency-dependent Scaling Behavior^a

IL	$n-G'(D_1)$	$n-G''\left(D_1\right)$	$n-G'(D_2)$	$n-G''(D_2)$
[EMIM][TFSI]	1.660 ± 0.120	1.030 ± 0.035		0.920 ± 0.031
[BMIM][TFSI]	1.359 ± 0.049	0.828 ± 0.027		0.659 ± 0.018
[HMIM][TFSI]	1.339 ± 0.081	0.762 ± 0.017		0.569 ± 0.030
[EMIM][FAP]	2.098 ± 0.204	0.808 ± 0.015	1.904 ± 0.212	0.729 ± 0.015
[EMIM][EtSO ₄]		0.887 ± 0.019		0.746 ± 0.048

"Power exponents (n) of the angular frequency $(\sim \omega^n)$ to fit the experimentally determined elastic and loss moduli.

$$x = z - \delta \tag{2}$$

and the relative velocity between the two surfaces is

$$V = \dot{x} - \dot{y} \tag{3}$$

Because the second surface is connected to a stiff spring that does not move laterally, the displacement *y* is 0, which yields

$$V = \dot{x} - \dot{y} = \dot{x} = \dot{z} - \dot{\delta} \tag{4}$$

$$K_x \times \delta - \eta \times \Omega \times (\dot{z} - \dot{\delta}) = 0 \tag{5}$$

This expression gives the viscosity of the nanoconfined liquid with the measured cantilever deflection and its change with time as $\eta = \frac{K_x \delta}{(\hat{z} - \hat{\delta})\Omega}.$

For a purely linear viscoelastic behavior and an input motion being a cosine function, $z=A_0\cos(\omega t)$, the deflection of the cantilever is given by $\delta=A_1\cos(\omega t+\phi)$, where ω is the angular frequency $(\omega=2\pi\nu)$, ν is the frequency, and ϕ is the phase difference. The parameters A_1 and ϕ are measured and converted to the rheological properties of the system by solving the equation of motion. Differentiating between real and imaginary components of the complex viscosity, $\eta=\eta'-i\eta''$, this gives

$$\eta'' = \frac{K_x}{\omega \Omega} \frac{f \cos(\phi) - 1}{f^2 + 1 - 2f \cos(\phi)} \tag{6}$$

$$\eta' = \frac{K_x}{\omega \Omega} \frac{f \sin(\phi)}{f^2 + 1 - 2f \cos(\phi)} \tag{7}$$

where η' is the real component (loss) and η'' is the imaginary component (elastic), $f=\frac{A_0}{A_1}$, $\Omega=\pi r^2/D$ for a plane–plane geometry, with r the radius of the flattened area (Figure 1C) and D the thickness of the nanoconfined IL film, or $\Omega=16/5\pi R'\log(2R'/D)$ for a sphere-plane geometry, where D is the separation at the point of closest approach and R' is the radius of the sphere. The magnitude of the complex viscosity (labeled as effective viscosity here) of the nanoconfined IL is obtained from

$$\eta_{\text{eff}} = \sqrt{{\eta'}_{\text{IL}}^2 + {\eta''}_{\text{IL}}^2} = \frac{K_x}{\omega \Omega (f^2 + 1 - 2f \cos(\phi))^{1/2}}$$
(8)

Storage and loss moduli are determined from the complex viscosity as

$$G_{\rm IL}' = \omega \eta'' \tag{9}$$

$$G_{II}'' = \omega \eta' \tag{10}$$

They are attributed to the moduli of the nanoconfined IL due to the negligible influence of other components as discussed later.

The strain rate is given as

$$\dot{\gamma} = \frac{V}{D} = i\omega \frac{A_0 - A_1 \exp(i\phi)}{D} \exp(i\omega t)$$
(11)

and its maximum value is

$$\dot{\gamma_0} = \frac{\omega \sqrt{(A_1 \sin \phi)^2 + (A_0 - A_1 \cos \phi)^2}}{D}$$
(12)

The maximum shear stress is thus determined from $\sigma_0 = \eta_{\text{eff}} \dot{\gamma}_0$.

We estimated the contribution of the glue to the viscoelastic response of the system by performing reference measurements in mica—mica contact. The rheological characteristics of the glue layer underneath mica are shown in Figure S2a. This plot shows a viscoelastic behavior at low frequencies, while the behavior is mostly elastic at frequencies higher than 0.05 Hz. To explicitly consider the influence of the glue, the mathematical treatment by Granick et al. 33 was applied to treat the experimental results. This approach demonstrates the negligible viscous contribution of the glue, in agreement with other works and deviating from Granick's results, likely due to the much thinner glue layer in our experiments (see details in the Supporting Information). Since the glue is predominantly elastic, its contribution is accounted for by including its influence in the gauge factor of the spring determined in mica—mica contact: $z = \Delta_{\rm glue} + \Delta_{\rm spring} = K_2' V_{\rm spring}$. The calibration provides $K_2' = 8.2 \times 10^{-5} \ {\rm m/mV}$.

In each experiment, the measured deflection is first analyzed via Fourier transform to filter out the frequency of interest and to evaluate the signal-to-noise ratio. Only if the latter is higher than 4, the results are further analyzed. The Fourier transform analysis also serves to search for higher-order harmonics that are characteristic of nonlinear behavior. The filtered signal is conducted using a code developed in MATLAB. Figure S3 illustrates the applied piezo motion and the measured deflection. The filtered signal is then synchronized with the piezo motion by accounting for a consistently 8 ms lag between the commencement of piezo motion and the time zero of the measurement.

The main sources of error are discussed next. If the signal-to-noise ratio is not sufficiently high, the data filtering and fitting procedure can lead to a maximum error in phase shift of ~ 0.5 ms, which is determined in calibration tests using a perfectly rigid metal cylinder holding the springs together. This error can be remarkable in the high-frequency regime. The geometry of the contact is roughly approximated by a Couette flow, although the real contact is not perfectly given by parallel plates, as shown in Figure 1C. This inevitably leads to an error in the magnitude of the estimated viscosity and moduli. However, we chose not to consider Reynold's model of lubrication for a sphere-flat contact because this model assumes uniform viscosity around the semisphere, and it has been shown that the increase of viscosity of the ILs only occurs in the confined region.

Statistical Analysis. Error bars have been determined as standard errors unless otherwise indicated. The standard error of the power exponent n is given in Table 1. The exponent and the standard error were determined from the fits of the linearized power law ω^n to the logarithm of the measured values of G' and G'', where n is the slope. A t-test of the slope n was carried out, and the p-value (for N between 10 and 20) is much smaller than 0.01 for each of the ILs. The error bars of the relaxation time and of the flow unit size were determined from the standard error of the cross point between G' and G''. The error bars of the relaxation time were determined from the standard error of the cross point between increasing G' and the initial plateau. The error bars of λ were determined from the standard error of the fitting parameter in Eyring's model. The models were applied to N between 10 and 20 for each of the ILs. The regression analysis of all the models applied provides regression coefficients R^2 better than 0.96.

RESULTS

Five ILs were selected (Figure 1A), all of them with imidazolium cations, albeit with different alkyl chain lengths, and three different anions. To perform nanorheological measurements,

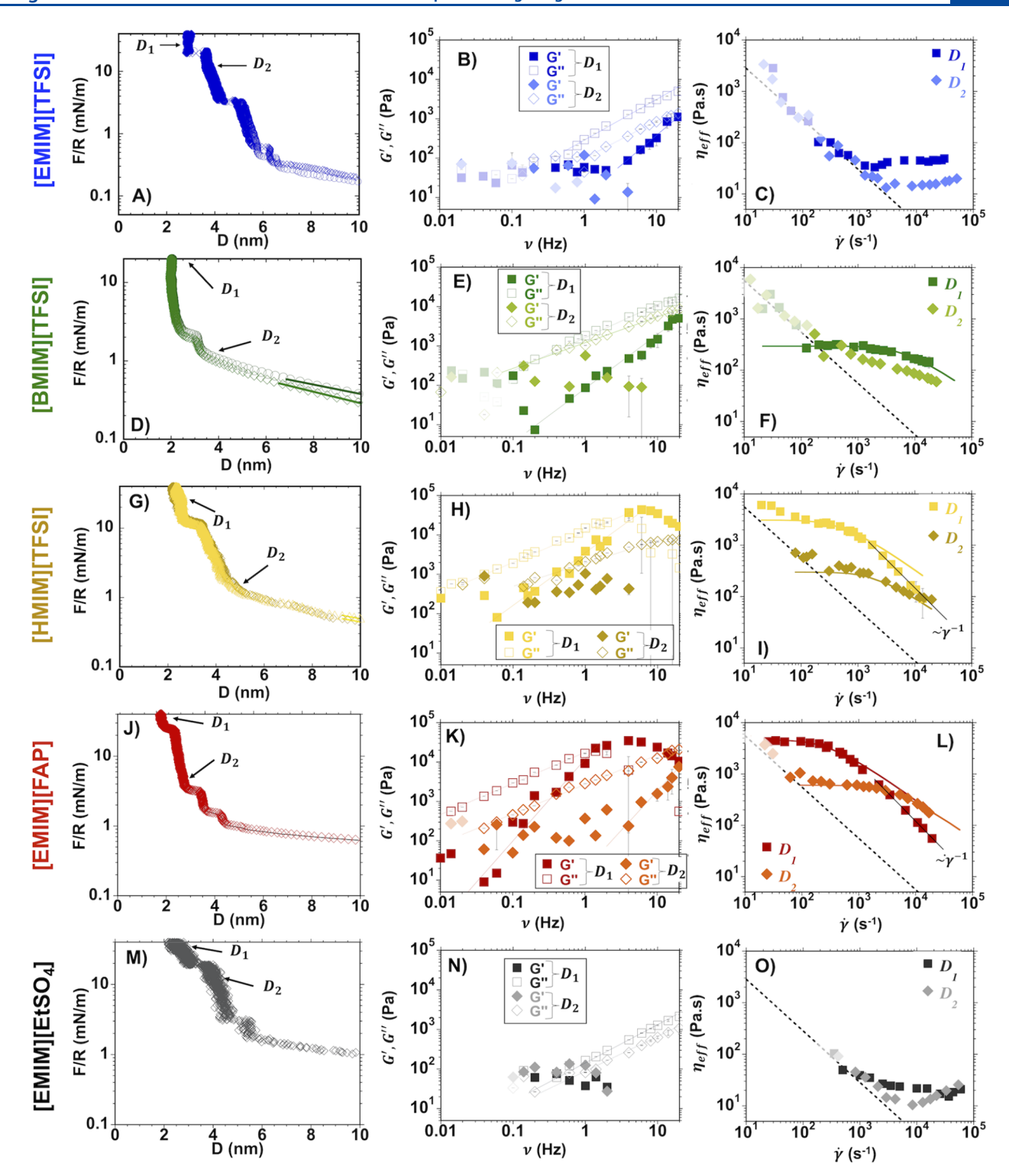


Figure 2. Surface forces and rheological measurements. Surface forces (left column), storage and loss moduli ($G'_{\rm IL}$ and $G''_{\rm IL}$, middle column), and effective viscosity (right column) of (A–C) [EMIM][TFSI], (D–F) [BMIM][TFSI], (G–I) [HMIM][TFSI], (J–L) [EMIM][FAP], and (M–O) [EMIM][EtSO_4], measured at D_1 (square) and D_2 (diamond). The lines show the fits to G' and G" according to a power law ω ", and the power exponents are shown in Table 1. The approximate positions of D_1 and D_2 are shown in the force—distance curves. The dashed lines were determined as $\sigma/\dot{\gamma}$, with shear stress $\sigma=K_2V_{\rm min}K_x/A_C$, where $V_{\rm min}$ is the precision of the strain gauges, roughly 0.00015 mV, and A_c is the area of contact. The force curves in the left column were adapted from ref 29. The bulk viscosity of the ILs is 33 mPa·s for [EMIM][TFSI], 42 61 mPa·s for [BMIM][TFSI], 42 81 mPa·s for [HMIM][TFSI], 42 71 mPa·s for [EMIM][FAP], 43 and 115 mPa·s for [EMIM][EtSO_4]. 44 The data points with less intense colors are those close to the detection limit and hence less reliable. The error bars for moduli and effective viscosity are often smaller than the marker size and therefore not visible.

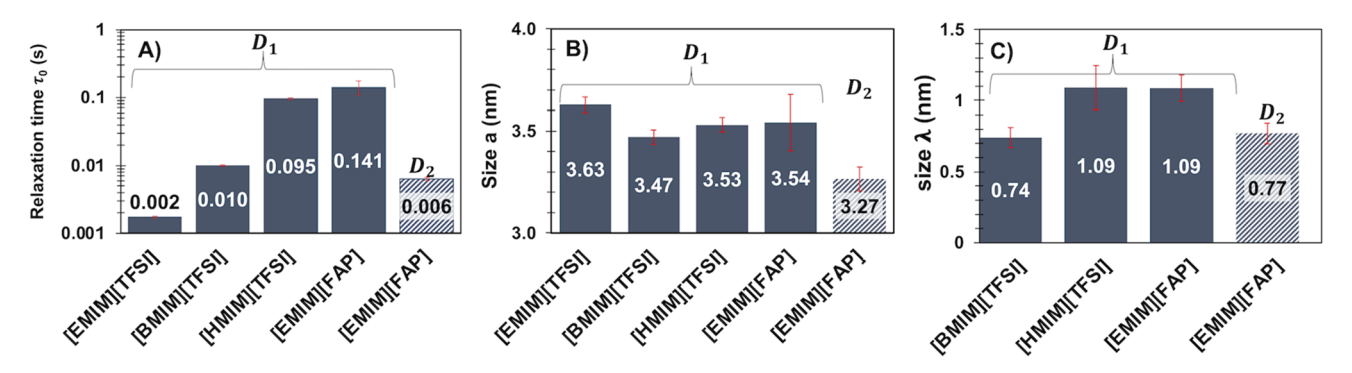


Figure 3. Characteristic times and lengths. (A) Characteristic relaxation time scale, $\tau_0 = 1/\omega_0$, at the cross point between G' and G'' for the selected ILs at D_1 and for [EMIM][FAP] also at D_2 (dashed bars); (B) size of the flow unit, a, calculated assuming diffusion-driven relaxation; (C) estimation of the shear-activation length λ based on Eyring's model to fit shear thinning behavior. The relaxation time $\tau_1 = 1/\omega_1$ at which the elastic modulus G' transitions from a plateau to $G' \sim \omega^2$ is shown in Figure S7.

our extended SFA was modified to a nanorheometer; the schematics are shown in Figure 1B and details of the instrument can be found in the Experimental section.

The SFA was first operated in the usual fashion to measure surface forces between mica surfaces in the five ILs. All measurements were conducted at 25 \pm 0.02 °C. Representative surface forces are shown in Figure 2 (left column) for the five ILs. The force-separation curves show steps characteristic of the squeeze-out of layers of IL ions while the mica surfaces are approached. Such steps in force-separation curves have been reported for several ILs previously (see review⁶ and refs. herein) and reflect the arrangement of IL ions in layers. This step size is not strictly equal to the true layer thickness but to the change in the film thickness when a layer is squeezed out of the thin film Δ ; we call this the layer thickness for conciseness. Although force measurements cannot reveal the layer composition, the average size of the steps in ILs with $[C_2C_1Im]$ and $[C_4C_1Im]$ cations (specifically, $\Delta \sim 0.76$ nm for $[C_2C_1Im][TFSI]$, $\Delta \sim 0.73$ nm for $[C_4C_1Im][TFSI]$, $\Delta \sim 0.77$ nm for $[C_2C_1Im][FAP]$, and $\Delta \sim 0.72$ nm for $[C_2C_1Im][EtSO_4]$) is consistent with a monolayer structure composed of both cations and anions alike (abbreviated as "monolayer"). MD simulations have reported similar values for Δ for $[C_2C_1Im][TFSI]$ and $[C_4C_1Im][TFSI]^{.39,40}$ For instance, the molecular volume Ω of [C2C1Im][TFSI] and [C4C1Im][TFSI] yields a length of $\Omega^{1/3}$ of ~0.74 and 0.75 nm, respectively. The larger size of the steps in [C₆C₁Im][TFSI] has been attributed to the squeeze-out of cation bilayers before; 41 here, the hexyl chains of two cation monolayers face each other forming a bilayer structure with intercalated counterbalancing anions (abbreviated as "bilayer"). The bilayers are quite compressible since the hexyl chains can interdigitate under applied compression, which justifies the smaller step size compared to the ion pair dimensions. Fewer layers are resolved in [BMIM][TFSI] and [HMIM][TFSI] (Figure 2D,G, respectively), compared to the ILs with [EMIM] cations. This suggests that either the longer alkyl chains disturb the layered arrangement of the IL ions or a slower approach velocity is needed to resolve these layers.^{29,30}

After these measurements, the IL was allowed to equilibrate at two different surface separations. First, the mica surfaces were approached to D_2 just before the last layer was resolved in the force—separation curves. To achieve this film thickness, a load needs to be applied, and the epoxy glue underneath the back-silvered mica deforms, leading to a smaller surface curvature. The radius of curvature (R') can be measured by scanning the glazing point of the spectrometer in two perpendicular

directions in the XY plane, while the thickness of the confined IL is continuously measured by the SFA. Two scan profiles in the X-direction are shown in Figure 1C. The flattened area is represented by the deviation from the spherical profile. After the nanorheological measurements at D_2 , the load was increased to approach the surfaces to a smaller distance, D_1 , and frequency and amplitude sweeps were repeated at this position. The thicknesses of the IL films $(D_1 \text{ and } D_2)$ were thus selected before and after the squeeze-out of the last resolved IL layer in surface force measurements. At the beginning of the rheological measurements at D_2 , the surface separation slightly varied, but it stabilized at the positions shown in Figure 2 just before the strong repulsion started. Repetition of the measurements led to slightly different values of D_1 and D_2 , but the results were consistent. For these reasons, we do not refer here to specific values of D_1 and D_2 , but the lines in Figure 2A,D,G,J,M indicate the approximate film thicknesses D_1 and D_2 , at which the rheological measurements were performed. The film thickness at which these measurements were conducted is thus different for each IL. Note that the films investigated with film thicknesses D₁ and D₂ are composed of more than one layer of IL ions.

In frequency-sweep tests, the frequency, ν , was varied from 0.01 to 20 Hz. The rheological analysis applied to these experimental data relies on the linear viscoelastic behavior of the nanoconfined ILs. Figure S4a shows the Fourier transform of the measured strain, which indicates the presence of higher-order harmonics at three times the applied frequency. The ratio of the intensity of the third harmonic to that of the first harmonic can be used to quantify the nonlinearity. ⁴⁵ A differentiation between the two intensity peaks is however only unambiguously possible at frequencies higher than 0.05 Hz. Figure S4b-f shows that this ratio is smaller than 10% for most of the data in films with a thickness of D_1 . Furthermore, amplitude sweeps were performed at four different frequencies. Figure S5 in the Supporting Information shows representative results for the selected ILs. The results demonstrate that the linearity varies with frequency and film thickness. The analysis discussed here corresponds to the data with an intensity ratio below 5%, which is assumed to be predominantly linear.

The middle column in Figure 2 shows the storage $G'_{\rm IL}$ and the loss moduli $G''_{\rm IL}$ of the five nanoconfined ILs at D_1 and D_2 . Both $G'_{\rm IL}$ and $G''_{\rm IL}$ of the five investigated ILs show clear dependence on the thickness of the confined film. For [EMIM][TFSI] at $D_1 \sim 2$ nm (squares), Figure 2B shows that $G'_{\rm IL}$ remains almost constant below a frequency of $\nu_1 \sim 2$ Hz (relaxation time $\tau_1 = 1/\omega_1 = 0.08$ s), after which $G'_{\rm IL}$ increases with frequency as

 $G_{\rm IL}^{\prime}\sim\omega^{1.95}$, while $G_{\rm IL}^{\prime\prime}$ increases according to $G_{\rm IL}^{\prime\prime}\sim\omega^{1.03}$, that is, almost linearly, with ω being the angular frequency. Similar trends with slightly different values for the power exponents and ν_1 are observed for [BMIM][TFSI], [HMIM][TFSI], and [EMIM][FAP] at D_1 in Figure 2E,H,K, respectively. The respective power exponents are summarized in Table 1. Hence, over a range of frequencies, these ILs exhibit a close-to terminal behavior characterized by $G^{\prime\prime}\sim\omega$ and $G^{\prime\prime}\sim\omega^2$, with $G^{\prime\prime}>G^{\prime\prime}$, representing a viscoelastic fluid.

The frequency at which $G'_{\rm IL}$ and $G''_{\rm IL}$ equal each other (ν_0) is obtained by either directly reading the cross point (e.g., for [HMIM][TFSI] and [EMIM][FAP]) or extrapolating the two curves (e.g., for [EMIM][TFSI] and [BMIM][TFSI]). For each IL, a relaxation time scale, τ_0 , is calculated by taking $1/\omega_0$, leading to $\tau_0=0.002$, 0.010, 0.095, and 0.141 s, for [EMIM][TFSI], [BMIM][TFSI], [HMIM][TFSI], and [EMIM][FAP] at D_1 , respectively; see Figure 3a. Above ν_0 , the elastic behavior of [HMIM][TFSI] and [EMIM][FAP] exhibits predominantly a solid-like behavior (G'>G''). We believe that in the case of [EMIM][TFSI] and [BMIM][TFSI], ν_0 is beyond the measurable range of our instrument, and therefore, we cannot examine their elastic behavior.

Films with only one more IL layer (D_2) display a drastically different behavior. In the case of [EMIM][TFSI], [BMIM]-[TFSI], and [HMIM][TFSI], $G_{\rm IL}^{"}$ is still seen to increase almost linearly with frequency, but it stays smaller than $G_{\rm IL}^{"}$ at D_1 . $G_{\rm IL}^{'}$ remains constant until a specific frequency, beyond which $G_{\rm IL}^{'}$ drops into the error range. This response points toward a more predominantly viscous behavior of the ILs at D_2 , in contrast to their evident viscoelastic behavior at D_1 . The constant value of $G_{\rm IL}^{'}$ is intriguing, and it has been related to a nonlinear response (see Luengo et al. $^{2.5}$) or to shear banding 46 for other systems. However, the shear stress in these measurements is close to the detection limit of our dynamic SFA (see Figure S6), and hence, we need to consider these results with caution.

In the case of [EMIM][FAP] at D_2 , $G'_{\rm IL} \sim \omega^2$ beyond a frequency of 0.06 Hz, and hence, the response is still viscoelastic. We expect the cross point between $G''_{\rm IL}$ and $G'_{\rm IL}$ to happen at frequencies beyond the measurable range ($\nu_0 \sim 25$ Hz by extrapolation), with a less significant solid-like behavior at D_2 compared to D_1 . The relaxation time scale τ_0 is determined to be ~ 6 ms for [EMIM][FAP], that is, smaller than that at D_1 . Longer relaxation times with a decrease in the number of layers have also been reported for a molecular liquid under confinement 32 and associated with a more prominent solid-like behavior.

Finally, the behavior of [EMIM][EtSO₄] (Figure 2N) at both selected film thicknesses $D_1 \sim 2$ nm and $D_2 \sim 4$ nm is similar: $G_{\rm IL}'$ remains constant before becoming immeasurable with an increase in frequency, while $G_{\rm IL}''$ increases linearly with frequency, with $G_{\rm IL}''$ at D_2 being smaller in magnitude than that at D_1 . In other words, this IL remains a viscous fluid under nanoconfinement under the same conditions as the other imidazolium ILs. Note that [EMIM][EtSO₄] has the highest bulk viscosity among the selected ILs.

The right column in Figure 2 shows the effective viscosity $\eta_{\rm eff}$ as a function of the strain rate amplitude $\dot{\gamma}$. The effective viscosity of the nanoconfined ILs is several orders of magnitude larger than the bulk viscosity; see bulk values in the figure caption. Overall, the drainage of one IL layer leads to a prominent change of the effective viscosity, and the change depends on the strain rate amplitude. The effective viscosity of [EMIM][TFSI] remains approximately constant at strain rates larger than $\sim 1000 \; {\rm s}^{-1}$ at both D_1 and D_2 (Figure 2C). This corresponds to

the predominantly viscous behavior described earlier (G'' > G'). The initial decrease of the effective viscosity with strain rate follows $\eta_{\rm eff} \propto \dot{\gamma}^{-1}$, corresponding to the range where G' is constant. This range falls close to the detection limit of the strain gauges (dashed line), and hence, it needs to be considered with caution; nevertheless, we discuss later a potential physical origin for this behavior. The behavior of [EMIM][EtSO₄] is similar, as shown in Figure 2O. For [BMIM][TFSI], a constant effective viscosity is measured at D_1 , followed by shear thinning as the strain rate increases (Figure 2F). The Newtonian plateau is less prominent at D_2 . In [HMIM][TFSI], the effective viscosity is found to decrease, plateau, and continue to decrease, as the strain rate amplitude increases, at both D_1 and D_2 . In [EMIM][FAP], the effective viscosity is constant at a low strain rate at D_1 , and then, it decreases significantly with an increase in the shear rate amplitude. At D_2 , an initial decrease is seen around the detection limit, followed by a plateau in η_{eff} . Shear thinning behavior is also observed at a high strain rate amplitude as in the case of D_1 , with a different decay rate.

Comparing the results for [EMIM][TFSI], [BMIM][TFSI], and [HMIM][TFSI], it appears that longer alkyl chains lead to an overall higher effective viscosity under confinement and to a change of the scaling behavior, as described above. A correlation between higher effective viscosity at the plateau (or close to the plateau) and longer relaxation time τ_0 is observed. Interestingly, while [EMIM][EtSO₄] exhibits the highest bulk viscosity among the selected ILs, it has the lowest effective viscosity under confinement. [EMIM][FAP] shows the highest effective viscosity and a scaling behavior (as a function of strain rate) closer to that of [HMIM][TFSI] but very different from the other three ILs with [EMIM]⁺ cations. Note that although the effective shear viscosity in this work is intrinsically different from the viscosity in squeeze-out experiments, ²⁹ we also observed an increase in viscosity in that earlier work for the same ILs.

DISCUSSION

Terminal Behavior at $\nu_1 < \nu < \nu_0$. As shown in Figure 2, a behavior close to terminal flow— $G''_{IL} \propto \omega$, $G'_{IL} \propto \omega^2$, and $G'_{IL} < G''_{IL}$ — is obvious for [EMIM][TFSI], [BMIM][TFSI], [HMIM][TFSI], and [EMIM][FAP] at $D_1 \sim 2-3$ nm in an intermediate frequency range $\nu_1 < \nu < \nu_0$. Here, each structural unit in the confined IL film is able to relax within the experimentally relevant time scale. Using the relaxation time scale, $\tau_0 = 1/\omega_0$ (Figure 3A), it is possible to roughly estimate the dimensions of the structural flow unit in the nanoconfined IL films. Assuming that translational diffusion is the main mechanism for relaxation in the shear direction, ⁴⁷ the diffusion coefficient D is related to the lattice size given by the structural unit of size a

$$D = \frac{a^2}{4\tau_0} \tag{13}$$

On the other hand, the diffusion coefficient D can be estimated via the Stokes—Einstein relation 48

$$D = \frac{k_{\rm B}T}{4\pi\eta a} \tag{14}$$

where $k_{\rm B}$ is the Boltzmann constant and T is the absolute temperature. This yields the size of the structural units

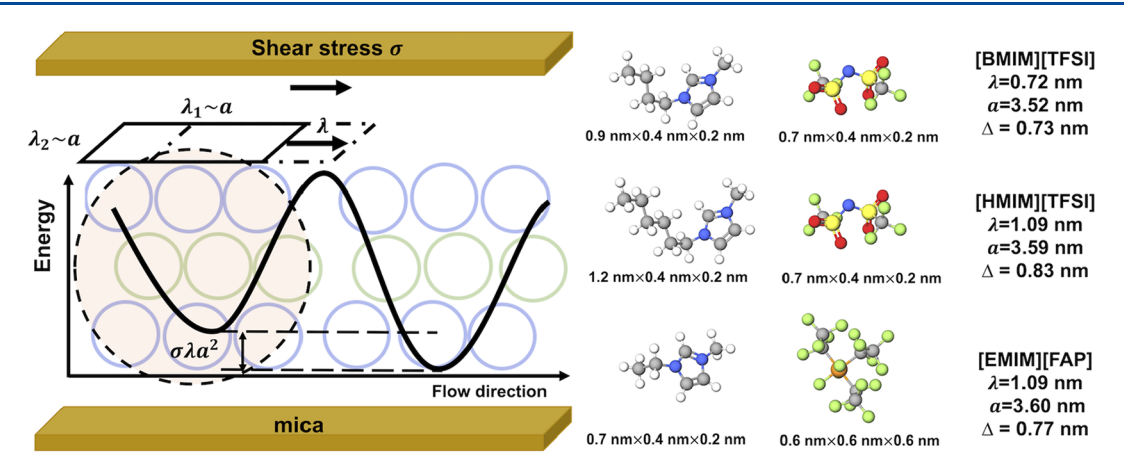


Figure 4. Illustration of the proposed flow behavior inferred from frequency-dependent shear rheology. The cations and anions are represented by blue and green circles, respectively. Oscillatory shear rheology suggests that IL ions form clusters with a characteristic length scale, a, similar to the film thickness. Under the theoretical framework proposed by Eyring, the shear-activation length, λ , represents the length scale over which shear stress works on the flow units to raise their energy level by $\lambda a^2 \sigma$, which helps overcome the energy barrier and thereby promotes motion. As a result, the three ILs exhibit a shear thinning behavior at intermediate frequencies. The molecular dimensions of [BMIM][TFSI], [HMIM][TFSI], and [EMIM][FAP] are determined in their unconfined states by molecular mechanics with the Avogadro software; the layer size Δ was reported in previous works²⁹ and is believed to be composed of ion pairs to preserve electroneutrality. The compressibility of the ionic structures is revealed by the difference between the ion-pair dimensions and the layer size. It is hypothesized that the shear-activation length, λ , is related to the compressibility. With similar sizes of flow units (a), λ is the governing factor for the effective viscosity of the nanoconfined ILs.

$$a = \left(\frac{\tau_0 k_{\rm B} T}{\pi \eta}\right)^{1/3} \tag{15}$$

The assumed value for η is determined as $\frac{G''}{\omega}$ in the plateau region (48, 314, 2840, and 4150 Pa·s for [EMIM][TFSI], [BMIM][TFSI], [HMIM][TFSI], and [EMIM][FAP] at D_1 , respectively; 239 Pa·s for [EMIM][FAP] at D_2). Figure 3b shows that the length scale a is similar for the selected ILs, despite the remarkable differences in effective viscosity and moduli and molecular structure. This indicates that the flow units of the ILs under nanoconfinement are similar in size. Counterintuitively, the size a exceeds that of individual ion pairs resolved by SFA and AFM for these ILs,6 suggesting the formation of supramolecular flow units. Such collective motion of molecules has been reported for molecular fluids and water. 32,34,35 In these works, the energy of Brownian motion, $k_{\rm B}T$, was normalized by the critical modulus G_c in the assumed Maxwell element to obtain a volume, k_BT/G_c , which is equivalent to tens or hundreds of molecules/ions. We note that this approach is equivalent to eq 15 because at a low frequency, $\eta \approx G_c \tau_0$ using the Maxwellian approach.

While our simplified model only provides the order of magnitude of the flow unit size, it is noteworthy that a is close to D_1 . The length scale a is determined from the relaxation by translation diffusion in the shear direction, and hence, it is less influenced by the dimension of the flow units in the perpendicular direction, which must be smaller than D_1 . It is thus possible that the flow units are anisotropic as a result of the one-dimensional confinement, but more precise information cannot be obtained from this model. We are aware that the validity of the Stokes-Einstein equation in confinement has been challenged⁴⁹⁻⁵¹ and that the assumption of translational diffusion could deviate from the true physics, and hence, this model provides a rough estimation of the effect of the molecular structure on the rheological behavior of the confined IL films. A fractional Einstein-Stokes law has been proposed to better describe imidazolium ILs in the bulk phase, with the viscosity

raised to a power of 0.9.⁵² However, this could not be verified to apply for ILs in their nanoconfined states.

Shear-Thinning Behavior and Liquid-Like Behavior. The effective viscosity of the nanoconfined IL films was often observed to decrease with strain rate beyond a plateau. Interestingly, MD simulations have shown such a decrease of the viscosity at much higher shear rates for another imidazolium IL $(10^7-10^9\ 1/s\ for\ [C_1C_1Im][TFSI]$ in the range of investigated pressures and temperatures of compared to the results for the nanoconfined ILs investigated here. This relation was modeled as a shear thinning behavior using Eyring's model. States that the shear thinning behavior originates from the shear-promoted flow as the work done by the applied shear stress reduces the energy barrier that needs to be surpassed for the flow unit to move to the next equilibrium location, illustrated in Figure 4. Eyring's model gives the following expression for the viscosity

$$\eta = \frac{2k_{\rm B}T}{V_{\rm act}} \frac{\sin h^{-1} (t_{\rm rel}\dot{\gamma})}{\dot{\gamma}} \tag{16}$$

where $t_{\rm rel}=1/\dot{\gamma}_{\rm E}$ is the characteristic relaxation time, $\dot{\gamma}_{\rm E}$ is the critical shear rate for the onset of shear thinning, and $V_{\rm a}$ is the shear-activation volume, which decreases the energy barrier by $\sigma V_{\rm act}$ with σ being the shear stress. Eyring introduced a shear-activation length λ , which represents the distance over which the shear force works on a flow unit. The relaxation time $t_{\rm rel}$ is related to a molecular relaxation time involved in the shear response.

The fits of eq 16 to the experimental results are shown for [BMIM][TFSI], [HMIM][TFSI], and [EMIM][FAP] in Figure 2F,I,L by lines with matching colors. We cannot exclude that [EMIM][TFSI] and [EMIM][EtSO₄] may exhibit shear thinning behavior at higher shear rates, but this was not probed here due to the limitation of the frequency range. Based on the previous discussion about the collective motion of the IL ions and the supramolecular structures, we assume the size of these structural units as a^2 and the shear-activation length as $\lambda \sim V_{\rm act}/a^2$. Note that λ_1 and λ_2 in Eyring's model are the dimensions of the flow unit parallel to the shear plane (see Figure 4), which are

assumed to be equal to a. The calculated values of λ are shown in Figure 3C. In the case of [HMIM][TFSI] and [EMIM][FAP] at D_1 , good agreement is only achieved at the initial decay, while significant deviations are observed with increasing shear rate. In this region, the data follow roughly a slope of -1 in the log—log plot, that is, $\eta_{\rm eff} \propto \dot{\gamma}^1$, which happens because the behavior is predominantly elastic (G' > G''). This was labeled as the "pure" tribological response of nanoconfined polymer melts by Luengo et al. ^{2.5} Hence, the values of λ have been obtained only in the region where the model fits well the experimental results.

The magnitude of λ is of similar order of magnitude as the estimated size of the structural unit based on translational diffusion, which gives us confidence that our interpretation of the collective motion of IL ions under confinement is correct. [HMIM][TFSI] and [EMIM][FAP] exhibit larger λ (~1.09 nm) compared to [BMIM][TFSI]. Using the framework of Eyring's model, a large activation length λ makes the flow unit capable of being strained to a larger extent before overcoming the energy barrier, that is, before flow happens. Interestingly, [HMIM][TFSI] has been shown to organize as cation bilayers (with anions to counterbalance charge) close to the mica surface, with the hexyl groups facing each other. 56 Under an applied load, the cation bilayers are significantly compressed. The [FAP] anion also bears flexible fluoroalkyl chains that may collapse under pressure. Furthermore, the smaller value of λ for [BMIM][TFSI] at D_1 suggests that smaller values of λ are associated with a more liquid-like behavior. This is also consistent with the smaller λ with an increase in film thickness for [EMIM][FAP] (1.09 vs 0.77 nm). The high ion compressibility of [EMIM][FAP] and [HMIM][TFSI] is supported by the size of the IL layers measured by SFA for the five ILs, ²⁹ which is smaller than the unconfined dimensions of [HMIM][TFSI] and [EMIM][FAP] (as shown in Figures 1A and 4). Based on this, we propose that the ion compressibility and the size of the structural flow units (a) are crucial in determining the transition from liquid-like to solid-like behavior in the response to shear of the confined ILs. The comparison of the relevant length scales is shown in Figure 4.

High-Frequency "Solid-like" Behavior ($\nu > \nu_0$). At frequencies $\nu > \nu_0$, two of the ILs, [HMIM][TFSI] and [EMIM][FAP], display predominantly elastic behavior ($G'_{\rm IL} > G''_{\rm IL}$) at D_1 , with $G''_{\rm IL}$ steadily decreasing. This indicates that [EMIM][FAP] and [HMIM][TFSI] are not capable of fully relaxing at high shear frequencies; note that these are the ILs with the longest relaxation time, τ_0 (Figure 3A). This suggests that the two ILs behave "solid-like" in this frequency range.

Low-Frequency Behavior. At small frequencies, the effective viscosity shows a power of ~ -1 dependence on strain rate, indicating that the shear stress $\sigma = \eta_{\text{eff}}$ remains constant. This coincides with the range over which G' remains approximately constant at low frequencies (Figure 2, middle column). Figure S6 shows the relaxation time τ_1 at which G' starts increasing with frequency. It is evident that the time scale increases with the length of the alkyl chain in the imidazolium cation and is higher for [EMIM][FAP], thus in agreement with the relaxation time τ_0 . While the low-frequency measurements could be influenced by the precision of the instrument, the differences observed across the investigated ILs indicate that there might be a physical origin for this behavior.

Plateaus for G' and G'' preceding the terminal behavior have been observed for nanoconfined polymer thin films, ²⁵ similar to the phenomenon observed in the present work. Such behavior was attributed to the presence of a yield stress above which the

thin film flows. For confined polymers, the yield stress increases upon a stronger confinement, that is, with a decrease in *D*. The yield-stress behavior of confined ILs has been reported before with a tuning-fork based rheological measurement. In our experiments, however, the sinusoidal input always leads to a sinusoidal output at such low frequencies, without any sign of truncation, although higher-order harmonics are detected with low intensity. This supports the absence of yield.

Shear banding is the observation that a complex (non-Newtonian) fluid under shear can undergo an instability that leads to a steady-state velocity profile with two different shear rates, a high shear rate linear profile near one wall coupled via an abrupt transition zone to a second lower shear rate linear profile near the other wall. The two regions are connected through an interfacial layer within which the shear stress is constant. 46 Experimental observations have shown unambiguous evidence of shear banding in solutions of worm-like micelles-namely, solutions of surfactants that have self-assembled into highly elongated, flexible structures that are entangled at concentrations where shear banding is observed. For worm-like micelles, it is shown that the shear stress does not increase monotonically with the increase of the shear rate but that there is a range of shear rates where the shear stress decreases. The unstable region appears in experiments often as a stress plateau.

Figure S6a,b shows the stress versus shear rate and the monotonic increase in stress with shear rate above a shear rate that depends on the IL, which coincides with the increase in G". Below this shear rate, the shear stress seems to decrease with shear rate for [EMIM][TFSI] and [EMIM][EtSO₄], while a quasi-plateau is observed for the other ILs, supporting both flow instability and shear banding. Furthermore, the shear stress appears often to oscillate between two values below the critical shear rate, and we speculate that this could be related to the instability of the flow. Therefore, the observed behavior could be related to shear banding. Shear banding has also been associated with birefringence. Figure S8 shows the refractive index and surface separation D for the five ILs during shear oscillation at 0.05 Hz compared to no oscillation at the same film thickness. The change in the refractive index does not unambiguously indicate the presence of birefringence during oscillatory shear

Master Curve. Figure 5 shows $G'_{\rm IL}$ and $G''_{\rm IL}$ for the investigated imidazolium ILs at D_1 and for [EMIM][FAP] also at D_2 as a function of the Deborah number $D_{\rm h} = \omega \tau_0$. The results for [EMIM][EtSO₄] are not shown here because τ_0 is unknown. The plot shows a good superposition of $G'_{\rm IL}$ and $G''_{\rm IL}$ and represents the proposed master curve for IL nanorheology. The high data scattering at low Deborah numbers correspond to the data points for G' and G'' obtained when the shear stress is close to the detection limit (less intense colors in Figure 2B,C,E,F). Note that this practice is analogous to the time—temperature superposition common in macroscopic rheology.

The master curve suggests that the rheological behavior of ILs exhibits three regimes under nanoconfinement: regime 1, at Deborah numbers (D_h) smaller than 0.01, where the storage modulus is seen to plateau; an intermediate regime characterized by a terminal behavior (regime 2); and regime 3 at Deborah numbers larger than 1, where the mechanical perturbation occurs on a time scale faster than the material can relax most of the stress. In regime 2, the IL behavior is prominently liquid, and the ion clusters relax under shear through translation diffusion. Comparison of the results for [EMIM][FAP] at D_1 and D_2 shows that squeezing out one IL

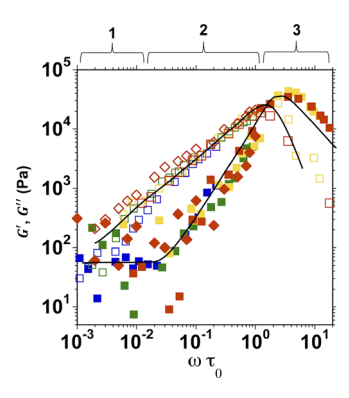


Figure 5. Nanorheology master curve. G' and G'' vs D_h constructed with data from [EMIM][TFSI] (blue), [BMIM][TFSI] (green), [HMIM][TFSI] (yellow), and [EMIM][FAP] (red) at D_1 , shown with red squares, and [EMIM][FAP] at D_2 , shown with red diamonds. The superposition of the data is achieved by defining the Deborah number as $D_h = \omega \tau_0$. As described in the text, three regimes with distinct nanorheological behavior are distinguished (labeled as 1, 2, and 3). The error bars are not shown for clarity but are the same as those shown in Figure 2 (middle column). The black lines in Figure 5 are intended to guide the eye.

layer promotes solid-like behavior. Note that the solid-like behavior can also be probed for [HMIM][TFSI], but it remains unexplored for the other ILs in the range of investigated frequencies. In the intermediate regime $0.01 < D_{\rm h} < 1$, the ILs exhibit shear thinning, except in the case of [EMIM][TFSI]. However, we cannot exclude that the onset of shear thinning was not probed because it happens at higher frequencies.

For a molecular liquid, octamethylcyclotetrasiloxane, it was possible to superpose the frequency-sweep measurements of confined films composed of up to seven layers onto a master curve.³² This is only possible here for [EMIM][FAP] with two different film thicknesses. For the other ILs, we found a change of behavior, which hinders this superposition; for example, for [EMIM][TFSI], [BMIM][TFSI], and [HMIM][TFSI], G' was not seen to increase in the range of investigated frequencies, and hence, the behavior remained overall viscous and τ_0 could not be determined. X-ray scattering has suggested that the Coulombic ordering of IL ions is partially disturbed under confinement, which alters the energetically preferred arrangement of the IL ions.⁵⁷ The anomalous capacitance of ILs in nanopores also suggests a confinement-induced change of the interionic interactions. 58,59 It is thus possible that ILs behave differently from molecular liquids, in that the squeeze-out of a layer essentially affects the interionic interactions, the nanostructure, and thus the rheological behavior.

[EMIM][EtSO₄] deserves special mention as the IL seems to remain a Newtonian liquid $(G'_{IL} \sim 0, G''_{IL} \sim \omega)$ even upon confinement to films with a thickness of 2 nm and despite its high bulk viscosity. Note that the hydrogen bonding capability in [EMIM][EtSO₄] is strong. This behavior was not observed for the other ILs, where hydrogen bonding is less prominent and interionic Coulombic, solvophobic, and steric forces dominate. It is thus possible that the prominent hydrogen bond network prevents the ions from rearranging upon nanoconfinement and helps maintain the fluid behavior. If this is the case, the enhancement of G'_{IL} induced by the drainage of layers of the other four ILs could be associated with enhanced interionic interactions (electrostatic, steric, and solvophobic), promoting the formation of clusters. The fact that the supramolecular cluster size (a) is similar for these ILs is also intriguing. We

hypothesize that this stems from the similar interionic interactions that drive the formation of the ion clusters (despite the different anion and/or alkyl length of the imidazolium cation) along with the compressibility of the ILs and the imposed confinement in the normal direction to a similar film thickness ($D_1 \sim 2{-}3$ nm).

The remarkable change of behavior in response to the applied frequency highlights the relevance of flow rates of ILs in nanopores and other confining geometries. For example, it has been reported based on simulations that fast charging leads to overall slower kinetics in ILs¹ due to ions being trapped in the transient crowded states, suggesting insufficient relaxation of the confined IL. This can be justified by the solid-like behavior reported in this work at a high frequency. We have also identified the IL compressibility to significantly influence the rheological behavior under confinement, and hence, this is a potential design parameter to achieve a targeted flow behavior. This new understanding from frequency-sweep measurements is also useful in reconciling reported measurements. For example, previous AFM- and SFA-based rheological studies were conducted around a single frequency 22-24,27,28,61 and the existence of a "solid-like" layer near the IL-solid interface could be induced by the high excitation frequency adopted in these instruments. We demonstrate here that there is a frequency threshold for the onset of the solid-like behavior and that it depends on the IL molecular structure.

CONCLUSIONS

In summary, we have studied the dynamic properties of five different imidazolium ILs under nanoconfinement via oscillatory shear measurements across 3 decades in frequency. The rheological properties change drastically as a function of the thickness of the nanoconfined ILs, as reflected in the distinct dependence of the storage and loss moduli on frequency and the remarkable increase of the effective viscosity. Through scrutiny of the rheological results, we show that [EMIM][TFSI], [BMIM][TFSI], [HMIM][TFSI], and [EMIM][FAP] form supramolecular clusters of similar sizes under strong confinement, and the compressibility of the ions seems to be responsible for the increase in viscosity in the confined state. A master curve for the storage and loss moduli of these ILs is obtained as a function of the Deborah number, suggesting the universality of the behavior of the nanoconfined ILs. A deviation from this behavior is observed in the case of [EMIM][EtSO₄], in which strong hydrogen bonding exists, which seems to restrict the reorganization of the confined IL in clusters and the slowdown of the dynamics.

We believe that this work advances the knowledge needed for the design of ILs with adequate rheological properties and thereby helps expand the range of applications of ILs in electrochemical devices and as lubricants. Further, the work calls for attention in the design and the choice of the best flow/ charging rate for IL-based energy storage devices as well as the optimal tribological conditions for IL lubricants to achieve optimal lubrication. Nevertheless, several questions remain to be answered, including the influence of trace amounts of solvents on the nanorheological properties of ILs. While the nanorheological studies were performed on selected imidazolium ILs. we expect the results and conclusion to hold true for other ILs with similar molecular structures and hence ion-ion interactions. Surface properties should play a role in the ion-surface interactions and thereby in the nanorheological properties. In the present work, the confining surface, mica, becomes

negatively charged in contact with the IL, and hence, electrostatic interactions between the IL and the surface are expected to influence the results. Extension of these studies to other dielectric surfaces (e.g., neutral, positively charged, or different chemical compositions) will provide insight into the role of ion—surface interactions on the nanorheological behavior of confined ILs. For electrochemical applications, studying the effect of a surface potential applied to metallic confining surfaces will be necessary. Furthermore, this work has focused on the one-dimensional confinement of several ILs, while the confinement in the nanopores of electrodes can also be two- and three-dimensional, and hence, additional confinement effects on the nanorheology of ILs are waiting to be unveiled.

ASSOCIATED CONTENT

5 Supporting Information

The Supporting Information is available free of charge at https://pubs.acs.org/doi/10.1021/acs.langmuir.1c03460.

Method to remove the influence of glue from rheology data; representative Fourier transform of the output waves; representative amplitude-sweep measurements; shear stress as a function of shear rate, relaxation times, refractive index, shear resonance frequency, storage and loss moduli of the epoxy glue layer underneath mica; and an example of experimental data recording and processing for [HMIM][TFSI] (PDF)

AUTHOR INFORMATION

Corresponding Author

Rosa M. Espinosa-Marzal — Department of Civil and Environmental Engineering at University of Illinois Urbana-Champaign, Urbana, Illinois 61801, United States; Department of Materials Science and Engineering, University of Illinois at Urbana—Champaign, Urbana, Illinois 61801, United States; orcid.org/0000-0003-3442-2511; Email: rosae@illinois.edu

Authors

Mengwei Han – Department of Civil and Environmental Engineering at University of Illinois Urbana-Champaign, Urbana, Illinois 61801, United States

Simon A. Rogers — Department of Chemical and Biomolecular Engineering, University of Illinois at Urbana-Champaign, Urbana, Illinois 61801, United States

Complete contact information is available at: https://pubs.acs.org/10.1021/acs.langmuir.1c03460

Funding

This material is based upon work supported by the National Science Foundation Grant CBET no. 19-16609 (to R.M.E-M.).

Notes

The authors declare no competing financial interest.

ACKNOWLEDGMENTS

The authors thank Prof. B. F. Spencer and S. Althaf V. S. (Department of Civil and Environmental Engineering) and Dr. K. A. Mechitov (Department of Computer Science) for their contribution to the development of the instrument. The authors also thank the assistance from Timothy J. Prunkard, Don Morrow, Dustin Brown, Jamar Brown, and Kyle Cheek at UIUC; Ken Sabino and Art Patton from Pacific Instruments; and Brian Connolly and Bill Machado from Physic Instrumente

for help in designing, manufacturing, and troubleshooting the nanorheometer.

REFERENCES

- (1) Breitsprecher, K.; Holm, C.; Kondrat, S. Charge Me Slowly, I Am in a Hurry: Optimizing Charge-Discharge Cycles in Nanoporous Supercapacitors. *ACS Nano* **2018**, *12*, 9733–9741.
- (2) Kondrat, S.; Wu, P.; Qiao, R.; Kornyshev, A. A. Accelerating charging dynamics in subnanometre pores. *Nat. Mater.* **2014**, *13*, 387–393.
- (3) Lian, C.; Janssen, M.; Liu, H.; van Roij, R. Blessing and Curse: How a Supercapacitor's Large Capacitance Causes its Slow Charging. *Phys. Rev. Lett.* **2020**, *124*, 076001.
- (4) Pak, A. J.; Hwang, G. S. Charging Rate Dependence of Ion Migration and Stagnation in Ionic-Liquid-Filled Carbon Nanopores. *J. Phys. Chem. C* **2016**, 120, 24560–24567.
- (5) Ye, C.; Liu, W.; Chen, Y.; Yu, L. Room-temperature ionic liquids: a novel versatile lubricant. *Chem. Commun.* **2001**, 2244–2245.
- (6) Espinosa-Marzal, R. M.; Han, M.; Arcifa, A.; Spencer, N. D.; Rossi, A. Ionic Liquids at Interfaces and Their Tribological Behavior. In *Encyclopedia of Interfacial Chemistry*; Wandelt, K., Ed.; Elsevier: Oxford, 2018; pp 172–194.
- (7) Monk, J.; Singh, R.; Hung, F. R. Effects of Pore Size and Pore Loading on the Properties of Ionic Liquids Confined Inside Nanoporous CMK-3 Carbon Materials. *J. Phys. Chem. C* **2011**, *115*, 3034–3042.
- (8) Rajput, N. N.; Monk, J.; Singh, R.; Hung, F. R. On the Influence of Pore Size and Pore Loading on Structural and Dynamical Heterogeneities of an Ionic Liquid Confined in a Slit Nanopore. *J. Phys. Chem. C* **2012**, *116*, 5169–5181.
- (9) Iacob, C.; Sangoro, J. R.; Kipnusu, W. K.; Valiullin, R.; Kärger, J.; Kremer, F. Enhanced charge transport in nano-confined ionic liquids. *Soft Matter* **2012**, *8*, 289–293.
- (10) Shi, W.; Sorescu, D. C. Molecular simulations of CO2 and H2 sorption into ionic liquid 1-n-hexyl-3-methylimidazolium bis-(trifluoromethylsulfonyl)amide ([hmim][Tf2N]) confined in carbon nanotubes. *J. Phys. Chem. B* **2010**, *114*, 15029–15041.
- (11) Atkin, R.; Warr, G. G. Structure in Confined Room-Temperature Ionic Liquids. *J. Phys. Chem. C* **2007**, *111*, 5162–5168.
- (12) Mezger, M.; Schröder, H.; Reichert, H.; Schramm, S.; Okasinski, J. S.; Schöder, S.; Honkimäki, V.; Deutsch, M.; Ocko, B. M.; Ralston, J.; Rohwerder, M.; Stratmann, M.; Dosch, H. Molecular layering of fluorinated ionic liquids at a charged sapphire (0001) surface. *Science* **2008**, 322, 424–428.
- (13) Perkin, S.; Albrecht, T.; Klein, J. Layering and shear properties of an ionic liquid, 1-ethyl-3-methylimidazolium ethylsulfate, confined to nano-films between mica surfaces. *Phys. Chem. Chem. Phys.* **2010**, *12*, 1243–1247.
- (14) Anaredy, R. S.; Shaw, S. K. Long-range ordering of ionic liquid fluid films. *Langmuir* **2016**, 32, 5147–5154.
- (15) Hohner, C.; Fromm, L.; Schuschke, C.; Taccardi, N.; Xu, T.; Wasserscheid, P.; Görling, A.; Libuda, J. Adsorption Motifs and Molecular Orientation at the Ionic Liquid/Noble Metal Interface: [C2C1Im][NTf2] on Pt(111). *Langmuir* **2021**, *37*, 12596–12607.
- (16) Chu, M.; Miller, M.; Douglas, T.; Dutta, P. Ultraslow Dynamics at a Charged Silicon-Ionic Liquid Interface Revealed by X-ray Reflectivity. *J. Phys. Chem. C* **2017**, *121*, 3841–3845.
- (17) Busch, M.; Hofmann, T.; Frick, B.; Embs, J. P.; Dyatkin, B.; Huber, P. Ionic liquid dynamics in nanoporous carbon: A pore-size- and temperature-dependent neutron spectroscopy study on supercapacitor materials. *Phys. Rev. Mater.* **2020**, *4*, 055401.
- (18) Forse, A. C.; Griffin, J. M.; Merlet, C.; Bayley, P. M.; Wang, H.; Simon, P.; Grey, C. P. NMR Study of Ion Dynamics and Charge Storage in Ionic Liquid Supercapacitors. *J. Am. Chem. Soc.* **2015**, *137*, 7231–7242.
- (19) Forse, A. C.; Griffin, J. M.; Merlet, C.; Carretero-Gonzalez, J.; Raji, A.-R. O.; Trease, N. M.; Grey, C. P. Direct observation of ion dynamics in supercapacitor electrodes using in situ diffusion NMR spectroscopy. *Nat. Energy* **2017**, *2*, 16216.

- (20) Uysal, A.; Zhou, H.; Feng, G.; Lee, S. S.; Li, S.; Cummings, P. T.; Fulvio, P. F.; Dai, S.; McDonough, J. K.; Gogotsi, Y.; Fenter, P. Interfacial ionic 'liquids': connecting static and dynamic structures. *J. Phys.: Condens. Matter* **2015**, *27*, 032101.
- (21) Uysal, A.; Zhou, H.; Feng, G.; Lee, S. S.; Li, S.; Fenter, P.; Cummings, P. T.; Fulvio, P. F.; Dai, S.; McDonough, J. K.; Gogotsi, Y. Structural Origins of Potential Dependent Hysteresis at the Electrified Graphene/Ionic Liquid Interface. *J. Phys. Chem. C* 2013, 118, 569–574.
- (22) Comtet, J.; Niguès, A.; Kaiser, V.; Coasne, B.; Bocquet, L.; Siria, A. Nanoscale capillary freezing of ionic liquids confined between metallic interfaces and the role of electronic screening. *Nat. Mater.* **2017**, *16*, 634–639.
- (23) Lainé, A.; Niguès, A.; Bocquet, L.; Siria, A. Nanotribology of Ionic Liquids: Transition to Yielding Response in Nanometric Confinement with Metallic Surfaces. *Phys. Rev. X* **2020**, *10*, 011068.
- (24) Krämer, G.; Bennewitz, R. Molecular Rheology of a Nanometer-Confined Ionic Liquid. *J. Phys. Chem. C* **2019**, *123*, 28284–28290.
- (25) Luengo, G.; Schmitt, F.-J.; Hill, R.; Israelachvili, J. Thin Film Rheology and Tribology of Confined Polymer Melts: Contrasts with Bulk Properties. *Macromolecules* 1997, 30, 2482–2494.
- (26) Bou-Malham, I.; Bureau, L. Nanoconfined ionic liquids: effect of surface charges on flow and molecular layering. *Soft Matter* **2010**, *6*, 4062–4065.
- (27) Ueno, K.; Kasuya, M.; Watanabe, M.; Mizukami, M.; Kurihara, K. Resonance shear measurement of nanoconfined ionic liquids. *Phys. Chem. Chem. Phys.* **2010**, *12*, 4066–4071.
- (28) Tomita, K.; Mizukami, M.; Nakano, S.; Ohta, N.; Yagi, N.; Kurihara, K. X-Ray diffraction and resonance shear measurement of nano-confined ionic liquids. *Phys. Chem. Chem. Phys.* **2018**, 20, 13714—13721.
- (29) Han, M.; Espinosa-Marzal, R. M. Electroviscous Retardation of the Squeeze Out of Nanoconfined Ionic Liquids. *J. Phys. Chem. C* **2018**, 122, 21344–21355.
- (30) Han, M.; Espinosa-Marzal, R. M. Influence of Water on Structure, Dynamics, and Electrostatics of Hydrophilic and Hydrophobic Ionic Liquids in Charged and Hydrophilic Confinement between Mica Surfaces. ACS Appl. Mater. Interfaces 2019, 11, 33465—33477.
- (31) Wang, Y.; Li, L. Uncovering the Underlying Mechanisms Governing the Solidlike Layering of Ionic Liquids (ILs) on Mica. *Langmuir* **2020**, *36*, 2743–2756.
- (32) Demirel, A. L.; Granick, S. Glasslike Transition of a Confined Simple Fluid. *Phys. Rev. Lett.* **1996**, 77, 2261–2264.
- (33) Granick, S.; Hu, H.-W. Nanorheology of confined polymer melts. 1. Linear shear response at strongly adsorbing surfaces. *Langmuir* **1994**, 10. 3857–3866.
- (34) Hu, H.-W.; Carson, G. A.; Granick, S. Relaxation time of confined liquids under shear. *Phys. Rev. Lett.* **1991**, *66*, 2758–2761.
- (35) Zhu, Y.; Granick, S. Viscosity of interfacial water. *Phys. Rev. Lett.* **2001**, 87, 096104.
- (36) Heuberger, M. The extended surface forces apparatus. Part I. Fast spectral correlation interferometry. *Rev. Sci. Instrum.* **2001**, *72*, 1700–1707.
- (37) Heuberger, M.; Vanicek, J.; Zäch, M. The extended surface forces apparatus. II. Precision temperature control. *Rev. Sci. Instrum.* **2001**, *72*, 3556–3560.
- (38) Ewoldt, R. H.; Hosoi, A. E.; McKinley, G. H. New measures for characterizing nonlinear viscoelasticity in large amplitude oscillatory shear. *J. Rheol.* **2008**, *52*, 1427–1458.
- (39) Wang, Y.; Tian, G. The Influence of Anion Structure on the Ionic Liquids/Au (100) Interface by Molecular Dynamics Simulations. *Langmuir* **2021**, *37*, 14059–14071.
- (40) Di Lecce, S.; Kornyshev, A. A.; Urbakh, M.; Bresme, F. Lateral ordering in nanoscale ionic liquid films between charged surfaces enhances lubricity. *ACS Nano* **2020**, *14*, 13256–13267.
- (41) Smith, A. M.; Lovelock, K. R. J.; Perkin, S. Monolayer and bilayer structures in ionic liquids and their mixtures confined to nano-films. *Faraday Discuss.* **2013**, *167*, 279–292.

- (42) Tariq, M.; Carvalho, P. J.; Coutinho, J. A. P.; Marrucho, I. M.; Lopes, J. N. C.; Rebelo, L. P. N. Viscosity of (C2-C14) 1-alkyl-3-methylimidazolium bis(trifluoromethylsulfonyl)amide ionic liquids in an extended temperature range. *Fluid Phase Equilib.* **2011**, 301, 22–32.
- (43) Nazet, A.; Sokolov, S.; Sonnleitner, T.; Makino, T.; Kanakubo, M.; Buchner, R. Densities, Viscosities, and Conductivities of the Imidazolium Ionic Liquids [Emim][Ac], [Emim][FAP], [Bmim][BETI], [Bmim][FSI], [Hmim][TFSI], and [Omim][TFSI]. *J. Chem. Eng. Data* **2015**, *60*, 2400–2411.
- (44) Fröba, A. P.; Kremer, H.; Leipertz, A. Density, refractive index, interfacial tension, and viscosity of ionic liquids [EMIM][EtSO4], [EMIM][NTf2], [EMIM][N(CN)2], and [OMA][NTf2] in dependence on temperature at atmospheric pressure. *J. Phys. Chem. B* **2008**, *112*, 12420–12430.
- (4S) Dötsch, T.; Pollard, M.; Wilhelm, M. Kinetics of isothermal crystallization in isotactic polypropylene monitored with rheology and Fourier-transform rheology. *J. Phys.: Condens. Matter* **2003**, *15*, S923–S031
- (46) Hu, Y. T.; Lips, A. Kinetics and mechanism of shear banding in an entangled micellar solution. *J. Rheol.* **2005**, *49*, 1001–1027.
- (47) Koenderink, G. H.; Zhang, H.; Aarts, D. G. A. L.; Lettinga, M. P.; Philipse, A. P.; Nägele, G. On the validity of Stokes-Einstein-Debye relations for rotational diffusion in colloidal suspensions. *Faraday Discuss.* **2003**, *123*, 335–354. ; discussion 401-21
- (48) Einstein, A. Investigations on the Theory of the Brownian Movement; Courier Corporation, 1956.
- (49) Faucheux, L. P.; Libchaber, A. J. Confined Brownian motion. *Phys. Rev. E: Stat. Phys., Plasmas, Fluids, Relat. Interdiscip. Top.* **1994**, 49, 5158–5163.
- (50) Köhler, M. H.; Bordin, J. R.; da Silva, L. B.; Barbosa, M. C. Breakdown of the Stokes-Einstein water transport through narrow hydrophobic nanotubes. *Phys. Chem. Chem. Phys.* **2017**, *19*, 12921–12927.
- (51) Mallamace, F.; Branca, C.; Corsaro, C.; Leone, N.; Spooren, J.; Stanley, H. E.; Chen, S.-H. Dynamical Crossover and Breakdown of the Stokes—Einstein Relation in Confined Water and in Methanol-Diluted Bulk Water. *J. Phys. Chem. B* **2010**, *114*, 1870—1878.
- (52) Harris, K. R. The fractional Stokes-Einstein equation: application to Lennard-Jones, molecular, and ionic liquids. *J. Chem. Phys.* **2009**, 131, 054503.
- (53) Voeltzel, N.; Vergne, P.; Fillot, N.; Bouscharain, N.; Joly, L. Rheology of an ionic liquid with variable Carreau exponent: A full picture by molecular simulation with experimental contribution. *Tribol. Lett.* **2016**, *64*, 1–12.
- (54) Powell, R. E.; Eyring, H. Mechanisms for the Relaxation Theory of Viscosity. *Nature* **1944**, *154*, 427–428.
- (55) Spikes, H.; Tysoe, W. On the Commonality Between Theoretical Models for Fluid and Solid Friction, Wear and Tribochemistry. *Tribol. Lett.* **2015**, *59*, 21.
- (56) Smith, A. M.; Lovelock, K. R. J.; Perkin, S. Monolayer and bilayer structures in ionic liquids and their mixtures confined to nano-films. *Faraday Discuss.* **2013**, *167*, 279–292.
- (57) Futamura, R.; Iiyama, T.; Takasaki, Y.; Gogotsi, Y.; Biggs, M. J.; Salanne, M.; Ségalini, J.; Simon, P.; Kaneko, K. Partial breaking of the Coulombic ordering of ionic liquids confined in carbon nanopores. *Nat. Mater.* **2017**, *16*, 1225–1232.
- (58) Feng, G.; Cummings, P. T. Supercapacitor Capacitance Exhibits Oscillatory Behavior as a Function of Nanopore Size. *J. Phys. Chem. Lett.* **2011**, *2*, 2859–2864.
- (59) Jiang, D.-e.; Jin, Z.; Wu, J. Oscillation of capacitance inside nanopores. *Nano Lett.* **2011**, *11*, 5373–5377.
- (60) Dhumal, N. R.; Kim, H. J.; Kiefer, J. Electronic structure and normal vibrations of the 1-ethyl-3-methylimidazolium ethyl sulfate ion pair. *J. Phys. Chem. A* **2011**, *115*, 3551–3558.
- (61) Garcia, L.; Jacquot, L.; Charlaix, E.; Cross, B. Nano-mechanics of ionic liquids at dielectric and metallic interfaces. *Faraday Discuss.* **2018**, 206, 443–457.